Journal Name

Dynamic Article Links ►

Cite this: DOI: 10.1039/c0xx00000x

www.rsc.org/xxxxxx

ARTICLE TYPE

High crystallinity Nb_3O_7F nanostructured photoelectrode: fabrication and photosensitisation

Haimin Zhang,[a] Yibing Li,[a] Yun Wang,[a] Porun Liu,[a] Huagui Yang,[a] Xiangdong Yao,[c] Taicheng An,[d] Barry J. Wood,[e] and Huijun Zhao*[a,b]

Received (in XXX, XXX) Xth XXXXXXXXX 200X, Accepted Xth XXXXXXXXX 200X

DOI: 10.1039/b000000x

High crystallinity Nb_3O_7F nanostructured film composed of bottom single crystal nanosheet layer with *ca.* 1.5 μm in thickness and top microsphere layer with *ca.* 18.5 μm in thickness has been successfully fabricated onto FTO conducting substrate through a facile and one-pot hydrothermal method. The top Nb_3O_7F microspheres with 2-5 μm in diameter are consisted of transparent single crystal nanosheets with 10-40 nm in thickness. Without need for further calcination, the as-synthesised Nb_3O_7F nanostructured films possess excellent crystallinity and highly mechanistic stability, which can be directly used as photoanodes for CdS quantum dot-sensitised solar cells (QDSSCs) and dye-sensitised solar cells (DSSCs). The transparent single crystal nanosheets constituted top Nb_3O_7F microspheres possess exposed (100) and (010) surfaces, which can play important role in sensitiser loading. The photoelectrochemical measurements indicate that CdS quantum dot-sensitised Nb_3O_7F nanostructured photoanode with seven chemical bath deposition (CBD) cycles (NbCdS-7) gives the best performance under visible light irradiation ($\lambda > 400$ nm) due to higher carrier concentration and longer electron lifetime in NbCdS-7. QDSSCs made of NbCdS-7 photoanodes show overall light conversion efficiency of 1.68%, which is almost 1.4 and 1.9 times of the NbCdS-5 and NbCdS-10 photoanodes, respectively. DSSCs measurement indicates that an overall light conversion efficiency of 2.78% can be achieved for the Nb_3O_7F nanostructured photoanode. This work exhibits a possibility of direct growth of high crystallinity metal oxide-based nanostructured film onto FTO conducting substrate as photoanode material without need for further calcination for solar energy conversion application.

1 Introduction

Titanium dioxide (TiO_2) has been the most widely investigated semiconductor material due to its excellent properties and extensive applications in photocatalysis, water splitting for generation of hydrogen, sensing, biomedicine, lithium-ion battery, and solar energy conversion.[1-11] Even so, considerable efforts have also been paid to develop other alternative materials such as ZnO, WO_3, SnO_2, and niobium-containing nanostructures for more extensive applications.[12-17] Amongst them, there is increasing interest in niobium-containing materials owing to their structural diversity and attractive applications for photocatalysis, gas sensing, lithium-ion battery, and solar cells.[15, 16, 18-21] To date, Nb_2O_5 with a wide bandgap of about 3.4 eV has been the most widely studied niobium-containing material because of its unique property and extensive applications.[15, 19, 20, 22] Varieties of synthetic methods have been employed to fabricate Nb_2O_5 nanostructures with different morphologies, such as nanoparticles, nanotubes, nanobelts and nanoforests, which have exhibited promising applications in different fields.[15, 19, 20, 22-24] However, only few studies on other forms of niobium-containing materials have been reported to date in literatures.[16, 21, 25-28] Very recently, our group developed a facile hydrothermal method to directly grow $Nb_3O_7(OH)$ single crystal nanorod film onto FTO substrate.[16] The fabricated $Nb_3O_7(OH)$ single crystal nanorods possess high crystallinity and large surface area, which can be directly used as photoanode for dye-sensitised solar cells (DSSCs) without need for further calcination to achieve an impressive overall light conversion efficiency of 6.77%.[16] This concept may be extended to fabricate high crystallinity metal oxide-based nanostructured film onto flexible substrate for flexible solar cell because the fabricated film does not need further calcination, thus avoiding the flexible substrate damage.

Several early reports have indicated that Nb_3O_7F is a class of important niobium-containing material with high crystallinity, which can be readily transformed into Nb_2O_5 with different crystal phases through thermal conversion.[25-31] In their studies, the Nb_3O_7F structures are usually obtained under the conditions of high temperature and high pressure.[25-31] In 1964, Andersson reported the synthesis of Nb_3O_7F by the reaction of Nb_2O_5 and NbO_2F under the conditions of high temperature and high pressure.[25] Their work confirms the Nb_3O_7F structure consists of blocks of the ReO_3-structure type which are fused together by means of octahedra sharing edges, with the unit-cell dimensions of $a = 20.67$ Å; $b = 3.833$ Å; $c = 3.927$ Å.[25] Permer *et al*. reported the synthesis of Nb_3O_7F structures by thermal decomposition of NbO_2F under high temperature and high pressure.[26, 31] In their studies, lithium ion-insertion into Nb_3O_7F structure and its thermal decomposition products were investigated in detail by various characterisation techniques.[26, 31] Their studies demonstrated that the one set of crystallographic shear planes in Nb_3O_7F can obviously slow down the Li-insertion reaction and stabilise the structure.[31] The study on thermal decomposition of the Li-inserted sample of $Li_{3x}Nb_3O_7F$ ($0 \leq x \leq 1.4$) exhibited various thermal decomposition products, such as LiF, NbO_2, $LiNb_3O_8$, and $LiNbO_3$.[26] Recently, Zhu *et al*. reported template free synthesis of 3D Nb_3O_7F hierarchical nanostructures.[21] The resulting product as photocatalyst exhibited good photocatalytic activity toward photocatalytic degradation of different dyes under UV irradiation.[21] To the best of our knowledge, the synthesised Nb_3O_7F structures in all reports to date are exclusively powder form, which have never been investigated as photoanode materials for photosensitisation.

Herein, we report for the first time a facile and one-pot hydrothermal method to directly grow high crystallinity Nb_3O_7F nanostructured films onto FTO conducting substrates. The obtained Nb_3O_7F nanostructured film is consisted of bottom single crystal nanosheet layer and top microsphere layer. The top microspheres are composed of transparent Nb_3O_7F single crystal nanosheets. The formation process of the as-synthesised Nb_3O_7F nanostructured film has been investigated and discussed in this work. The as-synthesised Nb_3O_7F nanostructured films possess excellent crystallinity and high mechanistic stability, which can be directly used as photoanodes for solar cells (CdS quantum dot-sensitised and dye-sensitised solar cells) without need for further calcination, displaying great potential as a promising photoanode material for solar energy conversion application.

2 Experimental section

Fabrication of Nb_3O_7F nanostructured film

In a typical synthesis, 0.5403 g of niobium (V) chloride ($NbCl_5$, Aldrich) was dissolved in 40 mL of 1.0% (v/v) hydrofluoric acid (HF, 48%, Sigma-Aldrich) solution. After ultrasonic treatment of 1 min, the resultant solution was transferred into a Teflon-lined stainless steel autoclave with a volume of 100 mL. Subsequently, a piece of pre-treated FTO conducting glass (15 Ω/square, Nippon Sheet Glass, Japan) with conductive facing up was immersed into the above solution. The hydrothermal reaction was carried out at 200 °C for 3 h. After reaction, the autoclave was cooled to room temperature and then FTO substrate was taken out, rinsed adequately with deionised water and allowed to dry in a nitrogen stream for further characterisation and measurement. The Nb_2O_5 nanostructured films were obtained by thermal treatment of high crystallinity Nb_3O_7F nanostructured films at 550 °C for 2 h.

CdS quantum dot sensitisation

CdS particles were deposited on the high crystallinity Nb_3O_7F nanostructured films by sequential chemical bath deposition (CBD) method.[32, 33] Typically, the Nb_3O_7F film was successively immersed in four different beakers for about 30 s in each beaker. One beaker contained 0.05 M $Cd(NO_3)_2$ solution, another contained 0.05 M Na_2S, and the other two contained distilled water to rinse the samples from the excess of each precursor solution. Such an immersion cycle was repeated 1, 3, 5, 7 and 10 times, and the obtained samples were denoted as NbCdS-1, NbCdS-3, NbCdS-5, NbCdS-7, and NbCdS-10, respectively. The resultant samples were tested in photoelectrochemical experiments and solar cells. For comparison, the Nb_2O_5 nanostructured films were also sensitised by CdS quantum dots with 7 CBD cycles as photoanodes for photoelectrochemical measurement.

Characterisation

SEM (JSM-7001F), TEM (Philips F20), and XRD (Shimadzu XRD-6000 diffractometer) were employed for characterising the fabricated samples. Chemical compositions of the samples were analysed by X-ray photoelectron spectroscopy (XPS, Kratos Axis ULTRA incorporating a 165 mm hemispherical electron energy analyzer). UV-vis diffuse reflectance spectra of the samples were recorded by a Varian Cary 5E UV-VIS-NIR spectrophotometer (Varian, US). The photoluminescent (PL) spectra of CdS quantum dot-sensitised samples were measured on F-7000 Fluorescence Spectrophotometer (Hitachi). Nitrogen adsorption-desorption isotherms of the samples were obtained on a Quantachrome Autosorb-1 surface area and pore size analyser.

Measurements

The photoelectrochemical experiments were carried out at 23 °C at a photoelectrochemical cell with a quartz window for illumination.[34] It consisted of a nanostructured photoanode, a saturated Ag/AgCl reference electrode, and a platinum mesh counter electrode. A voltammograph (CV-27, BAS) was used for the application of potential bias. Potential and current signals were recorded using a Macintosh (AD Instruments). The illuminated area of the photoanode was 0.785 cm^2. In photoelectrochemical experiments, 0.5 M Na_2S solution was used as the supporting electrolyte. Illumination was carried out using a 150 W Xe lamp (TrustTech, China). The wavelengths of the incident light were greater than 400 nm through a UV-400 filter. The intensity of the incident light was 100 mW/cm^2. For solar cell measurements, a series of cells were fabricated with traditional sandwich type configuration by using a CdS quantum dot-sensitised nanostructured film (or dye sensitised nanostructured film) and a platinum counter electrode. A mask with a window area of 0.15 cm^2 was applied on the photoanode film side to define the active area of the cells. A 500 W Xe lamp (Trusttech Co., Beijing) with an AM 1.5G filter (Sciencetech, Canada) was used as the light source. The Light intensity was measured by a radiant power meter (Newport, 70260) coupled with a broadband probe (Newport, 70268). The photovoltaic measurements of solar cells were recorded by a scanning potentiostat (Model 362, Princeton Applied Research, US). The electrolyte for CdS quantum dot-sensitised solar cell measurement contained 0.5 M Na_2S, 2 M S, and 0.2 M KCl. For dye-sensitised solar cell measurement, the electrolyte was DYESOL high efficiency electrolyte (EL-HPE). The IPCE as a function of wavelength was measured with QE/IPCE measurement kit (NewSpec). Impedance measurements were performed with a computer-controlled potentiostat (PAR2273, US). The frequency range is 0.1 Hz to 1 M Hz. The applied bias voltage and the magnitude of the modulation signal were set at open-circuit voltage of solar cells and 10 mV, respectively.

3 Results and discussion

Structural characteristics

Fig. 1A shows the XRD pattern of the as-synthesised sample, which can be indexed to an orthorhombic Nb_3O_7F structure with lattice parameters of a = 20.67 Å, b = 3.833 Å and c = 3.927 Å (JCPDS No. 74-2363).[21, 25, 28] Fig. 1B shows the surface SEM image of the as-synthesised sample, displaying a uniform microsphere film with the microsphere sizes of 2-5 µm in diameter. High magnification SEM image indicates that the obtained microsphere is composed of nanosheets with 10-40 nm in thickness (Fig. 1C). Interestingly, the cross-sectional SEM image reveals that the formed Nb_3O_7F nanostructured film consists of bottom nanosheet layer with 1.5 µm in thickness and top microsphere layer with 18.5 µm in thickness, as shown in Figs. 1D and E. The thickness of the whole film is about 20 µm. For solar energy conversion application, the bottom Nb_3O_7F nanosheet layer may play an important role in prohibiting electron leakage at the interfaces between FTO and microsphere layer, thus improving conversion efficiency.[35, 36] The diffuse reflection spectra of the Nb_3O_7F nanostructured film (Figure SI-1, ESI†) show higher reflectance in the wavelength range between 400 and 800 nm due to the large microsphere size, which can effectively improve sunlight utilisation efficiency of photoanode, and thus solar cell performance.[37] From this point of view, the fabricated Nb_3O_7F nanostructured film may have potential as photoanode candidate for solar energy conversion application. TEM image of an individual Nb_3O_7F nanosheet from ultrasound treated sample is given in Fig. 1F. The SAED pattern (top inset in Fig. 1F) and HRTEM image (bottom inset in Fig. 1F) reveal a good single crystalline nature of the Nb_3O_7F nanosheets. Moreover, the nanosheets are transparent. The SAED data confirm a preferred growth along [010] direction, while HRTEM image confirms the fringe spacings of 0.393 nm and 0.383 nm, which are consistent with the *d* values of (001) and (010) planes of the orthorhombic Nb_3O_7F, respectively.[25] Our experiments also demonstrate that the nanosheets originated from the bottom layer and top microspheres have same crystal structure. Fig. 1G schematically show the atomic configuration of the (100) and (010) planes of the Nb_3O_7F nanosheet. In previous study reported by other group, the oxygen and fluorine atoms are assumed to substitute each other in a random way in Nb_3O_7F crystal structure.[25] The structure of Nb_3O_7F consists of blocks of the ReO_3-structure type which are fused together by means of octahedra having edges in common (Fig. 1G).[25] Based on above results, the Nb_3O_7F nanosheets originated from top microspheres have (100) and (010) exposed planes, as shown in Fig. 1H. These exposed crystal planes could be advantageous to a further sensitiser loading (*e.g.*, CdS quantum dots).

In this work, the effect of different hydrothermal conditions on the resultant Nb_3O_7F morphology has been investigated. As shown in Figure SI-2 (ESI†), when the concentration of HF solution was set at 0.5% (v/v), only dispersed nanosheets were observed onto FTO substrate (Figure SI-2A, ESI†). Moreover, the formed nanosheet film possesses weakly mechanical stability and easy to peel off from FTO substrate. When the concentration of HF solution was increased to 3.0% (v/v), particle-shaped structures with an average diameter of 100 nm were observed onto FTO substrate (Figure SI-2B, ESI†), which could be due to the etching role of high concentration of HF.[38] Similarly, the formed film has weakly mechanical stability. Our experiments indicate that an optimum concentration of HF solution is 1.0% (v/v) for direct growth of high crystallinity Nb_3O_7F nanostructured film onto FTO substrate. Keeping other reaction conditions constant, the experiments of $NbCl_5$ concentration influence indicate that Nb_3O_7F nanostructured film onto FTO substrate can be formed in the concentration range of 0.03-0.06 M. Too low or too high concentration of $NbCl_5$ is not favorable to the formation of stable Nb_3O_7F nanostructured film (Figures SI-3A and B, ESI†). Further investigation demonstrates that high crystallinity Nb_3O_7F nanostructured film can be firmly formed onto FTO substrate at hydrothermal reaction temperature higher than 180 ºC (Figure SI-4B, ESI†). While at low hydrothermal reaction temperature (*e.g.*, 150 °C), only Nb_3O_7F microspheres assembled with nanorods can be observed (Figure SI-4A, ESI†). Compared to the Nb_3O_7F films formed at higher reaction temperature ($\geq$ 180 °C), the microsphere film obtained at 150 °C is not very firm and easy to peel off FTO substrate. To investigate the formation process of Nb_3O_7F nanostructured film obtained at 200 °C, the effect of hydrothermal reaction time was investigated in this work. When hydrothermal reaction time was set at 0.5 h, Nb_3O_7F nanoparticle film (Fig. 2A) started to form onto FTO substrate due to the hydrolysis of $NbCl_5$ precursor in HF solution to form Nb_3O_7F based on the following equations:[21]

$$NbCl_5 + 5H_2O \underset{200\ °C}{\overset{H^+}{\rightleftharpoons}} Nb(OH)_5 + 5HCl \qquad (1)$$

$$Nb(OH)_5 \xrightarrow{200\ °C} Nb_2O_5\downarrow + 5H_2O \qquad (2)$$

$$Nb_2O_5 + 2HF \xrightarrow{200\ °C} 2Nb_3O_7F\downarrow + H_2O \qquad (3)$$

With increasing hydrothermal reaction time, Nb_3O_7F concentration in reaction solution was further enhanced, which resulted in the formation of sphere-shaped structures onto FTO substrate (Fig. 2B). The formed Nb_3O_7F sphere-shaped structure composes of nanoparticles (Fig. 2B). When hydrothermal reaction time was set at 1.5 h, it was found that the size of the sphere-shaped structures was further increased (Fig. 2C). Importantly, the surface of the sphere-shaped structure started to form interlacedly connected streak structures at this reaction stage (Fig. 2C). Based on foregoing TEM analysis, the exposed crystal planes of the interlacedly connected streak structures should be (010) planes, which are favored to further growth of Nb_3O_7F nanosheets with a preferred growth along [010] direction. Further increasing reaction time to 2 h, nanosheet structures on Nb_3O_7F micropshere surface were obviously observed, as shown in Fig. 2D, indicating the growth of Nb_3O_7F nanosheets. Accompanying the growth of the top Nb_3O_7F microspheres, the bottom nanosheet layer also formed. High crystallinity Nb_3O_7F hierarchically structured film was firmly grown onto FTO substrate at hydrothermal reaction time of 3 h (Figs. 1B to E).

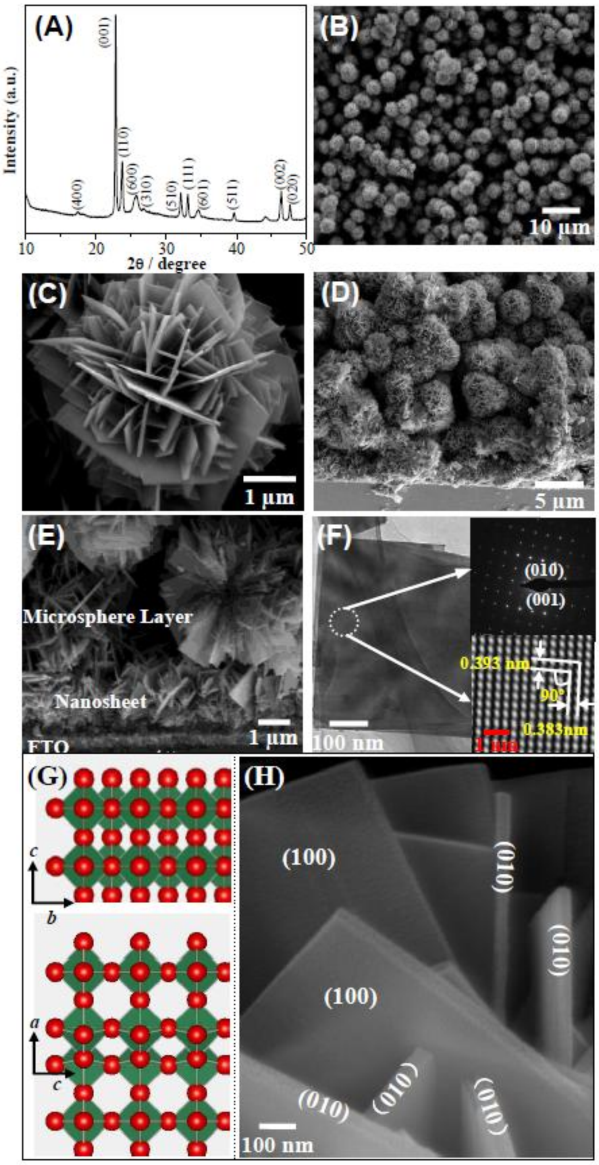

Fig. 1 (A) XRD pattern of the as-synthesised sample obtained in 40 mL of 1.0% (v/v) HF solution at 200 ºC for 3 h. (B) Surface SEM image of the as-synthesised Nb_3O_7F film. (C) High magnification SEM image of an individual Nb_3O_7F microsphere. (D) and (E) Cross-sectional SEM images of the obtained Nb_3O_7F nanostructured film. (F) TEM image of an individual Nb_3O_7F nanosheet with insets of SAED pattern (top) and HRTEM image (bottom). (G) Atomic structure models of Nb_3O_7F. Atom colour code: green-Nb, red-O, green octahedron: $[NbO_6]$. (H) High magnification SEM image of Nb_3O_7F nanosheets with exposed (100) and (010) planes.

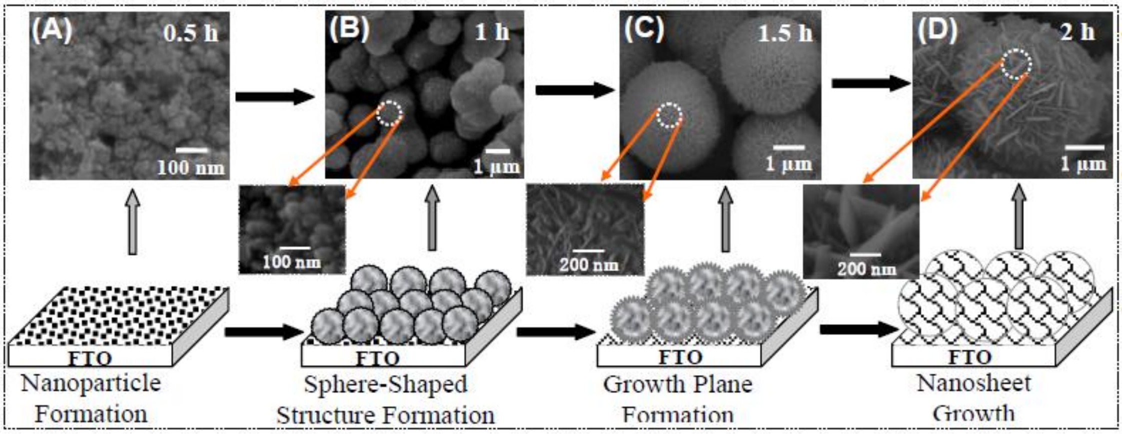

Fig. 2 Schematic illustration of the growth process of Nb_3O_7F nanostructured film onto FTO substrate.

CdS quantum dot sensitisation

Quantum dot-sensitised solar cells (QDSSCs) have attracted much attention because of their efficient charge separation, transport, and potential performance.[39, 40] To date, most studies on QDSSCs mainly focus on use of TiO_2 as photoanode material.[39-41] Without doubt, exploration of more alternative materials is highly desired to develop high performance QDSSCs. Recently, Kang *et al*. investigated Nb_2O_5 nanowire photoanode sensitised by a composition-tuned CdS_xSe_{1-x} shell for photoelectrochemical cells.[42] In comparison with TiO_2-CdS_xSe_{1-x} nanowire photoanode, Nb_2O_5-CdS_xSe_{1-x} nanowire photoanode exhibits excellent photoconversion efficiency.[42]

In this work, directly grown high crystallinity Nb_3O_7F nanostructured film onto FTO substrate was sensitised with CdS quantum dots by chemical bath deposition (CBD) method.[32, 33] During sensitisation, the CBD process was repeated up to *N* times (*N* = 1, 3, 5, 7, 10), and the corresponding electrodes are denoted as “NbCdS-*N*”. The CdS quantum dot-sensitised Nb_3O_7F nanostructured films as photoanodes were subsequently investigated in QDSSCs.

Fig. 3 shows the surface SEM images of CdS quantum dot-sensitised Nb_3O_7F films with different CBD cycles. It can be seen from Fig. 3 that some CdS crystallites begin to deposit on the nanosheets during initial cycles (*e.g.*, NbCdS-1, Fig. 3B). With further increasing CBD cycles, CdS crystallites form into aggregates of quantum dots, and more and more aggregates were observed on the surface of Nb_3O_7F nanosheets (Figs. 3C-E). After 10 CBD cycles, the whole Nb_3O_7F microsphere was almost completely covered by aggregates (NbCdS-10, Fig. 3F). Some studies have indicated that more CBD cycles can result in the growth of particle sizes of CdS aggregates, which can be disadvantageous to improving resultant solar cell performance.[43-45] Based on Fig. 3, it was also observed that CdS quantum dots are preferential to deposition on the top exposed (010) crystal planes of nanosheets within initial CBD cycles. With increasing CBD cycles, CdS particles appear on the (100) planes of Nb_3O_7F nanosheets. Fig. 3G shows TEM image of Nb_3O_7F nanosheet after depositing CdS quantum dots with 7 CBD cycles. Obviously, the exposed surface including (010) and (100) surfaces of nanosheet was uniformly covered by CdS particles, which can be beneficial to improving the resulting solar cell efficiency. HRTEM analysis (Fig. 3H) indicates that the observed 0.335 nm and 0.393 nm fringes correspond to the (111) plane of the cubic phase of CdS (JCPDS No. 65-2887) and the (001) plane of the orthorhombic Nb_3O_7F, respectively. The insets in Figs. 3A-F show the corresponding photographs of CdS quantum dot-sensitised Nb_3O_7F samples with different CBD cycles. It can be seen that the colour of the sample surface occurs obviously change from white for Nb_3O_7F sample without CdS sensitisation to light yellow, deep yellow, and orange yellow with increasing CBD cycles, suggesting the increase in the deposition amount of CdS quantum dots.[43]

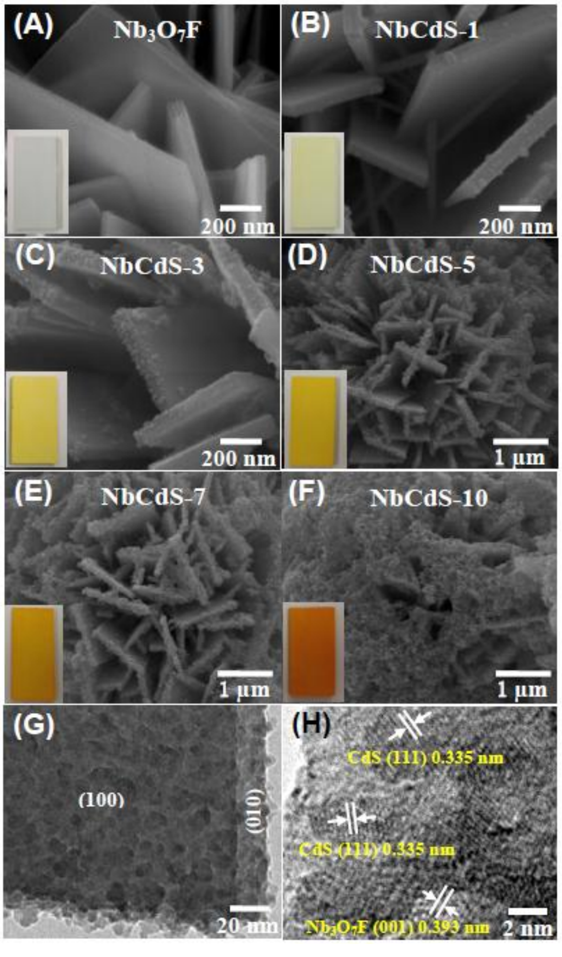

Fig. 3 (A) SEM image of the Nb_3O_7F nanostructured film before CdS sensitisation. (B)-(F) SEM images of the Nb_3O_7F nanostructured films with different CBD cycles. (G) TEM image of the Nb_3O_7F nanosheet after

CdS sensitisation with 7 CBD cycles. (H) HRTEM image of the Nb_3O_7F nanosheet after CdS sensitisation with 7 CBD cycles. The insets of their corresponding photographs.

UV-Vis diffuse reflection spectra of CdS quantum dot-sensitised samples show that the absorption edge of the samples happens to red shift with successive CBD cycles, which is mainly due to the increase of CdS particle size with increasing CBD cycles (Figure SI-5, ESI†).[43] In this work, we also performed energy dispersive spectroscopy (EDS) analysis for the samples before and after CdS sensitisation (Figure SI-6, ESI†). Obviously, compared to Nb_3O_7F sample (Figure SI-6A, ESI†), Cd and S elements appear in the EDS spectra after CdS deposition (take NbCdS-7 as an example) (Figure SI-6B, ESI†). Moreover, the molar ratio of Cd to S in NbCdS-7 sample is approximately 1:1, confirming stoichiometric formation of CdS.

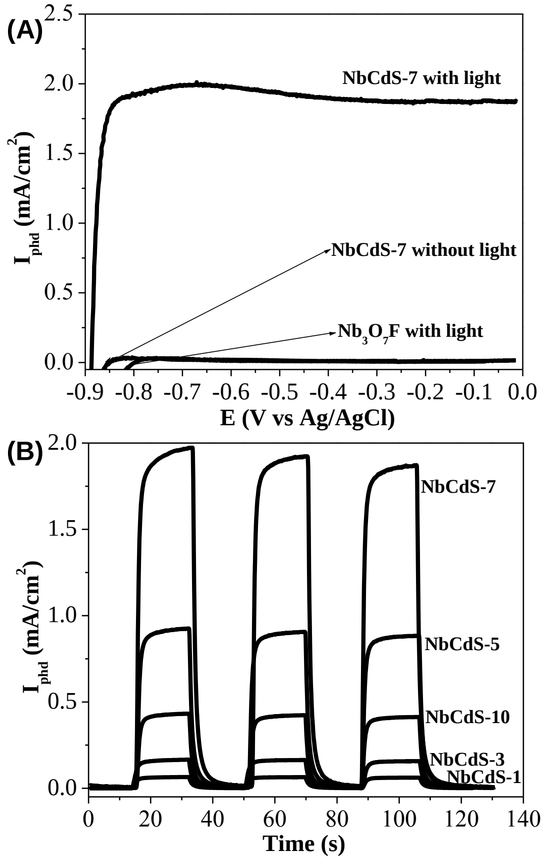

Fig. 4 (A) Voltammograms obtained from Nb_3O_7F and NbCdS-7 photoanodes in 0.5 M Na_2S supporting electrolyte solution. (B) Transient photocurrent responses of different NbCdS series photoanodes obtained at - 0.60 V of applied potential in 0.5 M Na_2S supporting electrolyte solution. Visible light intensity of 100 mW/cm^2.

Prior to evaluation of solar cell performance using NbCdS series photoanodes, the photoelectrochemical activity of the fabricated CdS-sensitised Nb_3O_7F nanostructured films as photoanodes was firstly measured in 0.5 M Na_2S supporting electrolyte under visible light irradiation ($\lambda > 400$ nm, light intensity = 100 mW/cm^2).[43] Fig. 4A shows the voltammograms of the photoanodes made of Nb_3O_7F and NbCdS-7 films in 0.5 M Na_2S supporting electrolyte. Apparently, no photocurrent response was observed for Nb_3O_7F photoanode under visible light irradiation. For NbCdS-7 photoanode without visible light irradiation, only a negligible dark current was observed. Under visible light illumination, NbCdS-7 photoanode exhibits good visible light response. Fig. 4B shows the transient photocurrent responses of the NbCdS series photoanodes obtained at -0.60 V (vs. Ag/AgCl) applied potential. Obviously, the NbCdS-7 photoanode was found to give the best photoelectrocatalytic activity in all investigated photoanodes. The increase in photocurrent response for NbCdS series photoanodes from NbCdS-1 to NbCdS-7 is mainly ascribed to the increase of CdS deposition amount with CBD cycles. Further increasing CBD cycles can result in further growth and formation of additional CdS particles to form thicker CdS particle film (*e.g.*, NbCdS-10). Although thicker CdS particle film may be beneficial to visible light utilisation, the recombination of photoelectrons and holes is more easy to occur, and thus decreasing the photocurrent response.[43] This has been further confirmed by photoluminescence (PL) spectrum. Many studies have indicated that PL analysis can be used to investigate the separation efficiency of photogenerated electrons and holes of photocatalysts.[46, 47] As shown in Figure SI-7 (ESI†), NbCdS-10 shows stronger PL intensity than that of NbCdS-7, indicating an improved recombination of photoelectrons and holes of NbCdS-10, and thus decreasing photocurrent response. The above results demonstrate that the photoanode with an apt CdS deposition amount can make the produced photoelectrons by CdS sites more effectively inject into the Nb_3O_7F, and thus improving visible light activity of the photoanode. This can be highly advantageous for photoelectrocatalytic and photovoltaic applications. For comparison, we also performed the photoelectrochemical experiments using the photoanode made from Nb_2O_5/CdS-7 (7 CBD cycles). The Nb_2O_5 film was firstly obtained by thermal treatment of Nb_3O_7F nanostructured film at 550 °C for 2 h. After calcination, the XRD pattern of the calcined sample can be indexed to Nb_2O_5, suggesting a structural transformation from orthorhombic Nb_3O_7F to monoclinic Nb_2O_5 (JCPDS No. 43-1042) (Figure SI-8A, ESI†). Compared to the XRD result obtained from the as-synthesised Nb_3O_7F sample, the calcined sample seems to have poor crystallinity owing to the rearrangement of crystal structure during calcination.[48] The SEM image of the calcined sample demonstrates that no obvious change in morphology has occurred after annealing, indicating high thermal stability of the nanosheet assembled microsphere structure (Figure SI-8B, ESI†). XPS data (survey spectrum) demonstrate that after annealing at 550 °C, fluorine element is completely disappeared, further indicating the structural transformation from orthorhombic Nb_3O_7F to monoclinic Nb_2O_5 (Figure SI-9, ESI†). Figure SI-10 (ESI†) shows the transient photocurrent responses of NbCdS-7 and Nb_2O_5/CdS-7 photoanodes at a -0.6 V (vs. Ag/AgCl) of applied potential. Obviously, the photocurrent response of NbCdS-7 photoanode is higher than that of Nb_2O_5/CdS-7 photoanode. This can be attributed to the decrease in crystallinity and surface area of Nb_2O_5 nanostructures after calcination.

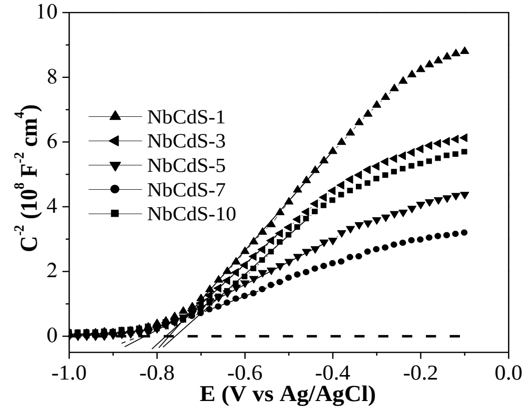

Fig. 5 Mott-Schottky plots of CdS sensitised Nb_3O_7F nanostructured photoanodes with different CBD cycles.

Fig. 5 shows Mott-Schottky plots of NbCdS series photoanodes under visible light irradiation (100 mW/cm^2). The slope of the tangent line in a Mott-Schottky plot is proportional to $1/N_D$ (N_D is the number of donors).[49] For NbCdS series photoanodes, the slope order is: NbCdS-7 < NbCdS-5 < NbCdS-10 < NbCdS-3 < NbCdS-1. This indicates that the order of the carrier concentration in NbCdS series photoanode films is of NbCdS-7 > NbCdS-5 > NbCdS-10 > NbCdS-3 > NbCdS-1. Higher carrier concentration means that more photoelectrons can be effectively transferred to external circuit in photoelectrocatalytic reaction, leading to higher photocurrent response. The above results are consistent with the results of photoelectrocatalytic experiments of NbCdS series photoanodes. Based on Mott-Schottky plots, the flat band potential of NbCdS-*N* photoanodes is approximate -0.87 V for NbCdS-7, -0.84 V for NbCdS-5, -0.79 V for NbCdS-10, -0.78 V for NbCdS-3, and -0.76 V for NbCdS-1, respectively (Fig. 5). Obviously, compared to other NbCdS photoanodes, the flat band potential of NbCdS-7 happens to negative shift. A negative shift of the flat band potential of photoanode can result in an increase in the open-circuit voltage of solar cells.[43]

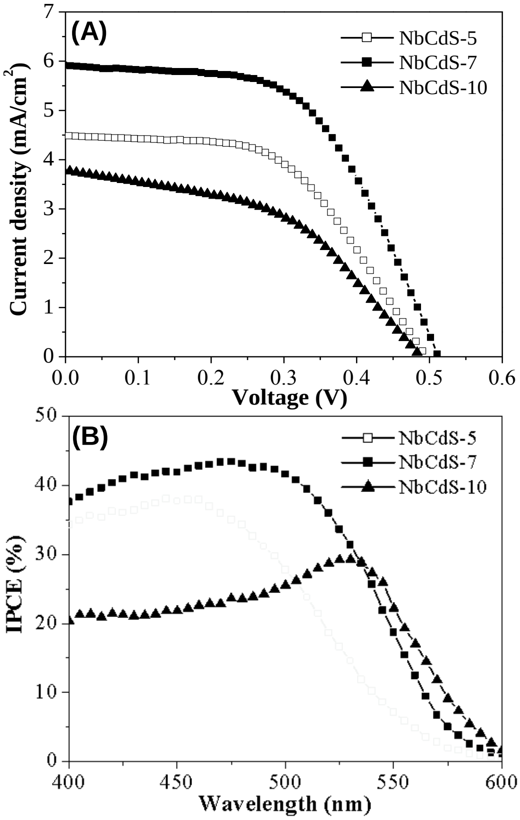

Fig. 6 (A) *J-V* characteristics of the NbCdS-5, NbCdS-7, and NbCdS-10 photoanodes. (B) Incident photon to current conversion efficiency (IPCE) curves of the NbCdS-5, NbCdS-7, and NbCdS-10 photoanodes.

In this work, we performed QDSSCs evaluation using NbCdS-5, NbCdS-7 and NbCdS-10 photoanodes as examples under the standard AM 1.5 simulated sunlight (100 mW/cm^2). Fig. 6A shows typical photocurrent density-photovoltage curves (J–V curves) of the resulting QDSSCs. Apparently, the NbCdS-7 photoanode possesses the highest short-circuit current densities (J_{sc}) of 5.91 mA/cm^2 that is almost 1.3 and 1.6 times of NbCdS-5 and NbCdS-10 photoanodes, respectively. The high photocurrent density of NbCdS-7 photoanode can be due to the higher carrier concentration generated in NbCdS-7 photoanode film in comparison with those in NbCdS-5 and NbCdS-10 photoanode films. A 511 mV of open-circuit voltage (V_{oc}) was obtained from the NbCdS-7 photoanode, which is 20 mV and 28 mV greater than those obtained from the NbCdS-5 and NbCdS-10 photoanodes. Compared to the NbCdS-5 and NbCdS-10 photoanodes, the higher V_{oc} of the NbCdS-7 photoanode is mainly ascribed to an apt CdS deposition amount on Nb_3O_7F nanostructured film causing the negative shift of the flat band potential, and thus resulting in V_{oc} improvement.[43] As a result, the NbCdS-7 photoanode exhibits overall light conversion efficiency of 1.68% that is almost 1.4 and 1.9 times of the NbCdS-5 and NbCdS-10 photoanodes, respectively. The key characteristics of these photoanodes are summarised in Table 1. Fig. 6B shows the IPCE spectra of NbCdS-5, NbCdS-7 and NbCdS-10 photoanodes. As shown in Fig. 6B, the NbCdS-7 photoanode displays the highest IPCE amongst all photoanodes, further confirming the significant role of an apt CdS deposition amount on Nb_3O_7F nanostructured film.

Table 1 Photovoltaic properties of the QDSSCs assembled with the NbCdS-5, NbCdS-7, and NbCdS-10 photoanodes.

Samples	J_{sc} (*mA/ cm*^{2})	V_{oc} (*mV*)	*FF* (%)	*η* (%)
NbCdS-5	4.48	491	53.5	1.18
NbCdS-7	5.91	511	55.6	1.68
NbCdS-10	3.77	483	47.2	0.86

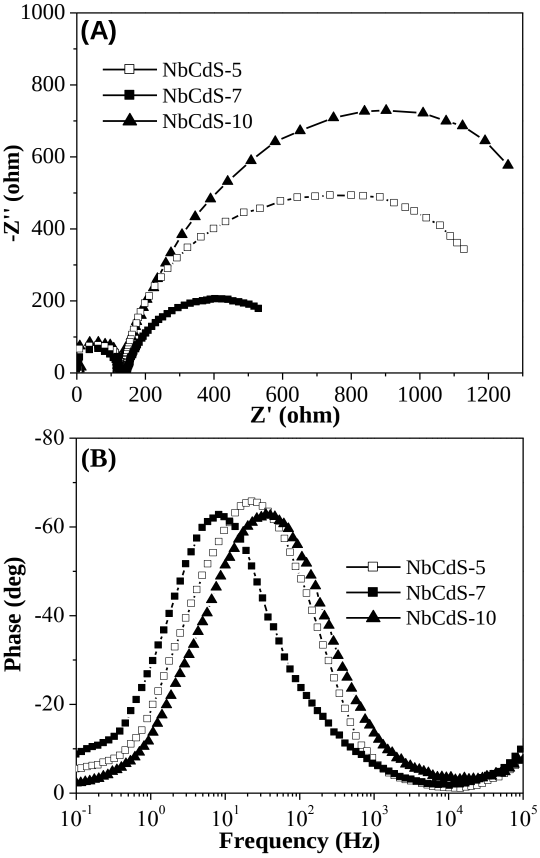

Fig. 7 Electrochemical impedance spectra (EIS) of QDSSCs assembled with the NbCdS-5, NbCdS-7, and NbCdS-10 photoanodes. (A) Nyquist plots of three films. (B) Bode-phase plots of three films.

The electron transport inside photoanode has an important influence on the resultant solar cell performance, which can be investigated by an electrochemical impedance spectroscopy (EIS) technique.[16, 33, 50] Fig. 7A shows the Nyquist plots of the QDSSCs assembled by the NbCdS-5, NbCdS-7 and NbCdS-10 photoanodes. As shown, a small and a large semicircle within high-frequency and middle-frequency regions were observed for all photoanodes, which is due to the electron transfer at the Pt/electrolyte interface (redox reaction of S^{2-}/S_x^{2-}) and the Nb_3O_7F/CdS/electrolyte interfaces, respectively. Obviously, Nyquist plots of all photoanodes indicate a charge transfer resistance order is of NbCdS-7 < NbCdS-5 < NbCdS-10. The electron lifetime (τ_n) in the CdS sensitised Nb_3O_7F nanostructured films can be estimated using $\tau_n = 1/2\pi f_{max}$, where f_{max} is the maximum frequency of the middle-frequency peak.[16] As shown in Fig. 7B, the f_{max} values are 8.3 Hz for NbCdS-7, 22.9 Hz for NbCdS-5, and 35.1 Hz for NbCdS-10, respectively. Correspondingly, the electron lifetime (τ_n) is calculated to be 19.2, 7.0 and 4.5 ms for the cells assembled by the NbCdS-7, NbCdS-5 and NbCdS-10 photoanodes, respectively. The above results further demonstrate that an apt CdS deposition amount on Nb_3O_7F nanostructured film can result in higher carrier concentration and longer electron lifetime, thus improving solar energy conversion efficiency.

Dye sensitisation

In our previous report, single crystal $Nb_3O_7(OH)$ nanorod film was directly grown onto FTO substrate by a facile hydrothermal method.[16] Without need for further calcination, the single crystal $Nb_3O_7(OH)$ nanorod film can be directly used as photoanode, showing an impressive solar energy conversion efficiency (η = 6.77%) owing to the high crystallinity and large surface area of nanorods.[16] In this work, high crystallinity Nb_3O_7F nanostructured film was also investigated in DSSCs. Without need for further calcination, the Nb_3O_7F nanostructured film as photoanode material was firstly sensitised with dye N719 (3×10^{-4} mol/L) for 24 h before DSSCs measurement. For comparison, the Nb_2O_5 nanostructured film obtained by thermal treatment of the Nb_3O_7F nanostructured film at 550 °C was also sensitised with dye N719 to investigate its DSSC performance. After calcination, the formed Nb_2O_5 nanostructured film possesses a thickness of *ca.* 18.6 μm. The decrease in film thickness compared to Nb_3O_7F film (*ca.* 20 μm) can be ascribed to the film structure collapse during high temperature calcination. This concurrently results in the decrease in the surface area of the calcined sample (BET = 26.1m^2/g) compared to the Nb_3O_7F sample (BET = 35.7 m^2/g). This may be not beneficial to high dye loading for the Nb_3O_7F film. Figure SI-11 (ESI†) shows the current-voltage characteristics of DSSCs assembled with the Nb_3O_7F and Nb_2O_5 photoanodes. As shown, the DSSCs assembled with the Nb_3O_7F photoanodes display a short-circuit current density (J_{sc}) of 6.02 mA/cm^2, an open-circuit voltage (V_{oc}) of 697 mV, a fill factor (*FF*) of 66.2% and an overall conversion efficiency (η) of 2.78%, whereas DSSCs assembled with Nb_2O_5 photoanodes possess a J_{sc} of 5.54 mA/cm^2, an V_{oc} of 686 mV, a *FF* of 55.3% and an overall conversion efficiency (η) of 2.10%. Comparison with Nb_2O_5 photoanodes, a 32.4% improvement in the overall conversion efficiency was achieved by using Nb_3O_7F photoanodes. Such a significant increase in overall conversion efficiency could be due to the high crystallinity and relatively large surface area of Nb_3O_7F nanostructures in comparison with Nb_2O_5 nanostructures. The above results demonstrate that the high crystallinity Nb_3O_7F nanostructured film can become a promising candidate as photoanode material for further improving DSSC performance.

It is well known that the matching of the conduction band energies between photoanode material and sensitiser plays a key role in the construction of high performance photovoltaics.[43] For this, we performed X-ray photoelectron valence-band (VB) spectra experiment of the as-synthesised Nb_3O_7F nanostructured film. Based on the UV-vis diffuse reflection spectra of the as-synthesised Nb_3O_7F nanostructured film (Fig. 8A), the band gap of 3.12 eV can be obtained for the Nb_3O_7F nanostructured film. The X-ray photoelectron valence band (VB) spectra reveal a VB maximum of *ca.* 1.94 eV for the Nb_3O_7F, which is very close to the VB value of TiO_2 (Fig. 8B).[51, 52] Due to similar values of band gap and valence band with TiO_2, the as-synthesised Nb_3O_7F should be suitable as a promising candidate for CdS quantum dot (dye)-sensitised solar cells from the point of view of the matching of the conduction band energies (Fig. 8C).

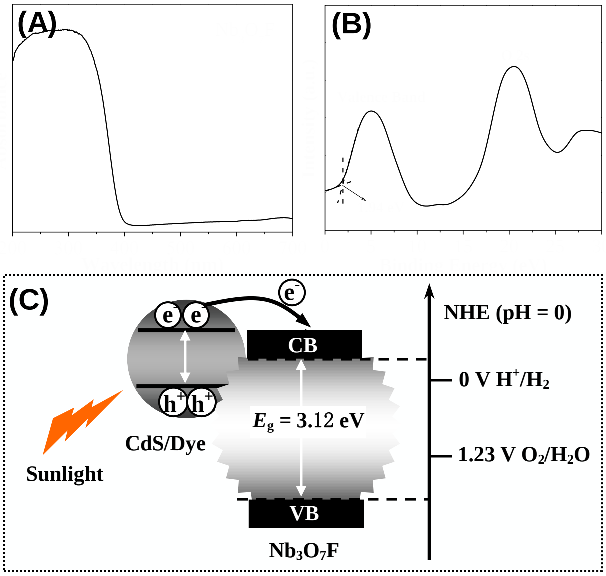

Fig. 8 (A) UV-vis absorption spectra of the as-synthesised Nb_3O_7F nanostructured film. (B) XPS valence band spectra of the as-synthesised Nb_3O_7F nanostructured film. (C) Determined valence band and conduction band edges of the as-synthesised Nb_3O_7F nanostructured film photoanode.

4 Conclusions

In summary, the high crystallinity Nb_3O_7F nanostructured films have been successfully fabricated onto FTO substrates through a facile and one-pot hydrothermal method. Without need for further calcination, the high crystallinity Nb_3O_7F nanostructured films can be directly sensitised with CdS quantum dots by chemical bath deposition (CBD) method. The resultant CdS quantum dot-sensitised Nb_3O_7F films with optimised CBD cycles (7 CBD cycles in our case) show excellent photoelectrocatalytic activity under visible light irradiation. An overall light conversion efficiency of 1.68% can be achieved from a quantum dot-sensitised solar cell (QDSSC) assembled with the NbCdS-7 photoanode. An apt CdS deposition amount on Nb_3O_7F nanostructures can produce high carrier concentration and long electron lifetime, thus resulting in excellent photoelectrocatalytic activity and relatively high QDSSC efficiency. Without need for further calcination, the high crystallinity Nb_3O_7F nanostructured films have also been investigated in dye-sensitised solar cells (DSSCs), exhibiting an overall light conversion efficiency of 2.78%. This study indicates feasibility for development of alternative photoanode materials for solar energy conversion application.

Notes and references

[a] *Centre for Clean Environment and Energy, Griffith University, Gold Coast Campus, QLD 4222, Australia. Fax: +61 7 55528067; Tel: +61 7 55528261; E-mail: h.zhao@griffith.edu.au*

[b] *Centre for Environmental and Energy Nanomaterials, Institutes of Solid State Physics, Chinese Academy of Sciences, Hefei 230031, China*

[c] *QLD Micro- and Nanotechnology Centre, Griffith University, Nathan Campus, QLD 4111, Australia*

[d] *State Key Laboratory of Organic Geochemistry, Guangzhou Institute of Geochemistry, Chinese Academy of Sciences, Guangzhou 510640, China*

[e] *Centre for Microscopy & Microanalysis, The University of Queensland, St Lucia, QLD 4072, Australia*

† Electronic Supplementary Information (ESI) available: Detailed characterisation, supporting images, UV-vis spectra, EDS analysis and PL measurement. See DOI: 10.1039/b000000x/

1. T. Nonoyama, T. Kinoshita, M. Higuchi, K. Nagata, M. Tanaka, K. Sato and K. Kato, *J. Am. Chem. Soc.*, 2012, **134**, 8841-8847.
2. X. Chen, S. Shen, L. Guo and S. S. Mao, *Chem. Rev.*, 2010, **110**, 6503-6570.
3. Y. Hou, X.-Y. Li, Q.-D. Zhao, X. Quan and G.-H. Chen, *Adv. Funct. Mater.*, 2010, **20**, 2165-2174.
4. J. Ng, S. Xu, X. Zhang, H. Y. Yang and D. D. Sun, *Adv. Funct. Mater.*, 2010, **20**, 4287-4294.
5. Y.-Y. Song, F. Schmidt-Stein, S. Bauer and P. Schmuki, *J. Am. Chem. Soc.*, 2009, **131**, 4230-4232.
6. J. S. Chen, Y. L. Tan, C. M. Li, Y. L. Cheah, D. Luan, S. Madhavi, F. Y. C. Boey, L. A. Archer and X. W. Lou, *J. Am. Chem. Soc.*, 2010, **132**, 6124-6130.
7. A. Hagfeldt, G. Boschloo, L. Sun, L. Kloo and H. Pettersson, *Chem. Rev.*, 2010, **110**, 6595-6663.
8. S. Yoriya, H. E. Prakasam, O. K. Varghese, K. Shankar, M. Paulose, G. K. Mor, T. J. Latempa and C. A. Grimes, *Sensor Lett.*, 2006, **4**, 334-339.
9. L. Yi, Y. Liu, N. Yang, Z. Tang, H. Zhao, G. Ma, Z. Su and D. Wang, *Energy Environ. Sci.*, 2013, **6**, 835-840.
10. X. Lai, J. E. Halpert and D. Wang, *Energy Environ. Sci.*, 2012, **5**, 5604-5618.
11. J. Du, J. Qi, D. Wang and Z. Tang, *Energy Environ. Sci.*, 2012, **5**, 6914-6918.
12. Q. Zhang, T. P. Chou, B. Russo, S. A. Jenekhe and G. Cao, *Angew. Chem., Int. Ed.*, 2008, **47**, 2402-2406.
13. G. Xi, J. Ye, Q. Ma, N. Su, H. Bai and C. Wang, *J. Am. Chem. Soc.*, 2012, **134**, 6508-6511.
14. J. Qian, P. Liu, Y. Xiao, Y. Jiang, Y. Cao, X. Ai and H. Yang, *Adv. Mater.*, 2009, **21**, 3663-3667.
15. C. Yan and D. Xue, *Adv. Mater.*, 2008, **20**, 1055-1058.
16. H. Zhang, Y. Wang, D. Yang, Y. Li, H. Liu, P. Liu, B. J. Wood and H. Zhao, *Adv. Mater.*, 2012, **24**, 1598-1603.
17. Z. Dong, X. Lai, J. E. Halpert, N. Yang, L. Yi, J. Zhai, D. Wang, Z. Tang and L. Jiang, *Adv. Mater.*, 2012, **24**, 1046-1049.
18. A. G. S. Prado, L. B. Bolzon, C. P. Pedroso, A. O. Moura and L. L. Costa, *Appl. Catal., B*, 2008, **82**, 219-224.
19. X. Fang, L. Hu, K. Huo, B. Gao, L. Zhao, M. Liao, P. K. Chu, Y. Bando and D. Golberg, *Adv. Funct. Mater.*, 2011, **21**, 3907-3915.
20. A. Le Viet, M. V. Reddy, R. Jose, B. V. R. Chowdari and S. Ramakrishna, *J. Phys. Chem. C*, 2010, **114**, 664-671.
21. Z. Wang, J. Hou, C. Yang, S. Jiao, K. Huang and H. Zhu, *Phys. Chem. Chem. Phys.*, 2013, **15**, 3249-3255.
22. A. Le Viet, R. Jose, M. V. Reddy, B. V. R. Chowdari and S. Ramakrishna, *J. Phys. Chem. C*, 2010, **114**, 21795-21800.
23. R. Ghosh, M. K. Brennaman, T. Uher, M.-R. Ok, E. T. Samulski, L. E. McNeil, T. J. Meyer and R. Lopez, *ACS Appl. Mater. Interf.*, 2011, **3**, 3929-3935.
24. P. Guo and M. A. Aegerter, *Thin Solid Film.*, 1999, **351**, 290-294.
25. S. Andersson, *Acta Chem. Scand.*, 1964, **18**, 2339-2344.
26. L. Permer, *J. Solid State Chem.*, 1992, **97**, 105-114.
27. K. A. Wilhelmi, L. Jahnberg and S. Andersson, *Acta Chem. Scand. (1947-1973)*, 1970, **24**, 1472-1473.
28. F. Huang, Z. Fu, W. Wang, H. Wang, Y. Wang, J. Zhang, Q. Zhang, S. W. Lee and K. Niihara, *Mater. Res. Bull.*, 2010, **45**, 739-743.
29. L. A. Bursill, *J. Solid State Chem.*, 1973, **6**, 195-202.
30. R. Gruehn, *Z. Anorg. Allg. Chem.*, 1973, **395**, 181-190.
31. L. Permer, *Chem. Commun., Univ.*, 1991, 51.
32. W.-T. Sun, Y. Yu, H.-Y. Pan, X.-F. Gao, Q. Chen and L.-M. Peng, *J. Am. Chem. Soc.*, 2008, **130**, 1124-1125.
33. L. Li, X. Yang, J. Gao, H. Tian, J. Zhao, A. Hagfeldt and L. Sun, *J. Am. Chem. Soc.*, 2011, **133**, 8458-8460.
34. D. Jiang, H. Zhao, S. Zhang and R. John, *J. Catal.*, 2004, **223**, 212-220.
35. J. Xia, N. Masaki, K. Jiang and S. Yanagida, *Chem. Commun.*, 2007, 138-140.
36. J. Kim and J. Kim, *J. Nanosci. Nanotechnol.*, 2011, **11**, 7335-7338.
37. H. Zhang, Y. Han, X. Liu, P. Liu, H. Yu, S. Zhang, X. Yao and H. Zhao, *Chem. Commun.*, 2010, **46**, 8395-8397.
38. Y. Wang, H. Zhang, Y. Han, P. Liu, X. Yao and H. Zhao, *Chem. Commun.*, 2011, **47**, 2829-2831.
39. M. Gratzel, *Nature*, 2001, **414**, 338-344.
40. P. K. Santra and P. V. Kamat, *J. Am. Chem. Soc.*, 2012, **134**, 2508-2511.
41. P. V. Kamat, *J. Phys. Chem. C*, 2008, **112**, 18737-18753.
42. J. H. Kang, Y. Myung, J. W. Choi, D. M. Jang, C. W. Lee, J. Park and E. H. Cha, *J. Mater. Chem.*, 2012, **22**, 8413-8419.
43. D. R. Baker and P. V. Kamat, *Adv. Funct. Mater.*, 2009, **19**, 805-811.
44. K. Kumar Challa, S. K. Goswami, E. Oh and E.-T. Kim, *Appl. Phys. Lett.*, 2011, **99**, 153111/153111-153111/153113.
45. E. Hong, J. H. Kim, S. Yu and J. H. Kim, *Korean J. Chem. Eng.*, 2011, **28**, 1684-1687.
46. G. Liao, S. Chen, X. Quan, H. Yu and H. Zhao, *J. Mater. Chem.*, 2012, **22**, 2721-2726.
47. K. Selvam and M. Swaminathan, *RSC Adv.*, 2012, **2**, 2848-2855.
48. F. Izumi and H. Kodama, *Z. Anorg. Allg. Chem.*, 1978, **441**, 196-204.
49. F. Spadavecchia, G. Cappelletti, S. Ardizzone, M. Ceotto and L. Falciola, *J. Phys. Chem. C*, 2011, **115**, 6381-6391.
50. S. H. Kang, S.-H. Choi, M.-S. Kang, J.-Y. Kim, H.-S. Kim, T. Hyeon and Y.-E. Sung, *Adv. Mater.*, 2008, **20**, 54-58.
51. H. Zhang, X. Liu, Y. Li, Q. Sun, Y. Wang, B. J. Wood, P. Liu, D. Yang and H. Zhao, *J. Mater. Chem.*, 2012, **22**, 2465-2472.

52. J. Pan, G. Liu, G. Q. Lu and H.-M. Cheng, *Angew. Chem., Int. Ed.*, 2011, **50**, 2133-2137.